Chemotherapy and adjuvant therapies' impact on the internal remodeling process of bone and its mechanical behavior for breast cancer patients

Imane Ait Oumghar, Abdelwahed Barkaoui, Tarek Merzouki, Daphné Guenoun, Patrick Chabrand

Chemotherapy and adjuvant therapies' impact on the internal remodeling process of bone and its mechanical behavior for breast cancer patients

Imane Ait Oumghar[1,2] | **Abdelwahed Barkaoui**[1] | **Tarek Merzouki**[3] | **Daphne Guenoun**[2] | **Patrick Chabrand**[2]

[1]Laboratoire des Energies Renouvelables et Matériaux Avancés (LERMA), Université Internationale de Rabat, Rabat, Morocco

[2]Institut des Sciences du Mouvement (ISM), Université Aix-Marseille, Marseille, France

[3]Laboratoire d' Ingénierie des Systèmes de Versailles LISV, IUT de Mantes en Yvelines Université de Versailles Saint-Quentin, Mantes-La-Jolie, France

Abstract

Breast cancer is a significant public health issue affecting women worldwide. While advancements in treatment options have led to improved survival rates, the impact of breast cancer and its treatments on bone health cannot be overlooked. Bone remodeling is a complex process regulated by the delicate balance between bone formation and resorption. Any disruption to this balance can lead to decreased bone density, increased fracture risk, and compromised physical function. To investigate the effects of breast cancer and its treatments on bone remodeling, a finite element model was developed in this study. This model incorporated bone remodeling equations to simulate the mechanical behavior of bone under different conditions. The ABAQUS/UMAT software was used to simulate the behavior of bone tissue under the influence of breast cancer and treatments. Our findings suggest that bone loss is more pronounced after secondary breast cancer and treatment, leading to bone loss (6%–19% decrease in BV/TV), reduced bone stimulation, and decreased effectiveness of physical activity on recovery. These results highlight the importance of early intervention and management of bone health in breast cancer patients to mitigate the negative impact of cancer and treatment on bone remodeling.

KEYWORDS

bone, bone density, breast cancer, finite element modeling, mechanobiology

1 | INTRODUCTION

Bone tissue serves as a dynamic and living composite material with crucial functions such as shielding the soft tissues from external forces, facilitating the release of calcium and other ions into the extracellular fluid, and providing support for hemopoiesis. The mechanical functionality of bones is maintained through a process known as bone remodeling, which enables the adaptation of the bone tissue to external loadings.[1,2] However, breast cancer (BC) and its treatments can disrupt this process and lead to adverse effects on bone health. Research suggests that breast cancer and its treatments can alter the bone remodeling process, leading to an imbalance between bone resorption and formation, ultimately resulting in bone loss and increased risk of fractures.[3]

Bone tissue deterioration due to BC and its treatments is caused by disruptions to bone metabolism, which is regulated by the biochemical process of bone remodeling (BR). BR involves osteoclasts and osteoblasts interacting in basic

multicellular units (BMUs), with the process being activated by mechanosensory bone cells called osteocytes. The RANKL/RANK/OPG pathway, consisting of RANK, RANKL, and OPG molecules, controls osteoclast differentiation and activation during BR. RANK-RANKL binding stimulates osteoclastogenesis, while OPG-RANKL binding protects the bone from excessive resorption by preventing RANK-RANKL binding.[4]

Over the past few decades, the finite element (FE) method has become increasingly popular in the fields of biomechanical engineering and regenerative medicine.[5] Utilizing FE modeling of human bones has proven to be a valuable tool for evaluating a broad range of outcomes in a consistent and replicable way. These models are based on medical images and offer a wealth of information about bone quality and mechanical capabilities. Furthermore, they can be used to create FE models that simulate the mechanobiological behavior of bones via the bone remodeling process. In authors[6] have proposed a method for predicting the effects of denosumab, a drug used to treat osteoporosis, on bone remodeling. The method combines pharmacokinetics (study of drug absorption, distribution, and metabolism) and finite element modeling (FEM). Based on the FE model results, bone mineral density (BMD) values of the proximal femur after have shown good consistency with experimental studies,[7-9] which shows that FEM approach could help improve the clinical management of osteoporosis and other bone-related conditions. In a more recent study,[10] have presented a new mathematical model that integrates mechanical and chemical factors for bone remodeling. The model considers various cell types, extracellular matrix, and signaling molecules involved in bone remodeling and simulates the dynamic behavior of the process, predicting the effects of different mechanical and chemical stimuli on bone tissue using FEM. Based on the results, the authors concluded that the FE model used in this study is capable of producing results that align with those obtained from previous research, as well as with clinical and experimental scenarios.

Building on our previous works[4,11] which were principally dedicated to mathematical modeling of bone remodeling under BC and BC treatments effect, this paper delves deeper into the mechanical behavior of bone under breast cancer and its treatment effects at the macroscopic level. Our previous study utilized mathematical modeling to understand the underlying mechanisms of breast cancer/ treatments-bone remodeling cells interactions. To present a proof of concept of our models, we utilized computational simulations using Abaqus/UMAT aiming to analyze the mechanobiological behavior of a real femur under BC and its treatments. By conducting several simulations, we were able to examine the potential differences in bone density and damage distribution between four different cases: (i) normal bone remodeling, (ii) bone remodeling under primary breast cancer, (iii) bone remodeling under secondary breast cancer, and (iv) bone remodeling under chemotherapy, tamoxifen, and aromatase inhibitor effect.

2 | FINITE ELEMENT MODELING OF BONE REMODELING

2.1 | Patient

Being among the most bone parts affected by cancer, we have chosen the proximal femur to simulate cancer and treatments' effect on bone. In our study, bone geometry of proximal femur was acquired from CT images of a healthy 73 aged women.

2.2 | Ethics statement

The proximal femur scans used in this research were obtained from the Radiology Department of the AP-HM (Assistance Publique-Hôpitaux de Marseille), specifically from Sainte-Marguerite Hospital in Marseille, France. The study protocol, including the use of these scans, was ethically reviewed, and approved under the registration number PADS23-121.

The authors declare that this report does not contain any personal information that could lead to the identification of the patient.

2.3 | Three-dimensional reconstruction of bone geometry

The first step to create the finite element model is to consider the three-dimensional the bone geometry (Figure 1). From patient CT images, segmentations and 3D reconstructions have been done to obtain the proximal femur geometry using the segmentation software Materialise Mimics. Segmentation is the operation where we extract, from grayscale

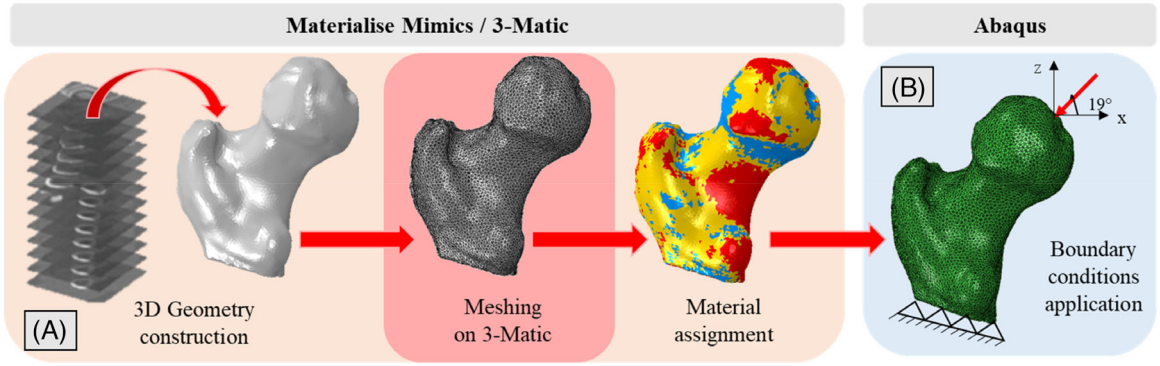

FIGURE 1 (A) Three-dimensional reconstruction of bone geometry and material assignment. The process is subdivided into 3 parts: (i) Construction of 3D geometry from patient's scans on Mimics, (ii) Meshing the 3D geometry on 3-Matic, (iii) and assignment of material properties of bone on Mimics (B) Boundary conditions applied on the created 3D geometry in Abaqus.

images, our region of interest (ROI) called mask. CT images are composed of voxels assigned to different gray shades. The gray levels of those voxels are expressed in Hounsfield Units (HU). Based on HU values, the tissue density is determined. A value of −1024 HU corresponds to air, 0 HU corresponds to water, and value greater than 1000 HU correspond to bone, calcium, and metal.[12] In order to extract our mask, each voxel in the image is assigned to the value 1 if it is in the ROI and 0 if it is not. The segmentation of a bone starts by: (i) thresholding the volumetric imaging by including all the voxels with values ranging between 226 and 2000 HU that correspond to bone HU values; (ii) separating the targeted bone zone from the other bone zones while keeping the initial mask containing all the bone tissue to be segmented; (iii) refining the mask to precisely match the outline of the bone. For this step, the filling of internal holes and morphological operations of erosion and dilation are carried out. Depending on the quality of the scanned images, it may be necessary to manually add or remove voxels that may or may not be part of the ROI.

2.3.1 | Material assignment

After defining our ROI and constructing our 3D geometry of the proximal femur, we have applied the mechanical properties, again using Materialise Mimics. This software permits to assign ash density for every HU value of the voxels using empirical function. In our case, we have used the formulations proposed by Sternheim et al.,[13] which permits to determine (i) K2HPO4 density of HU values (Equation 1), (ii) ash density as function of HU values (Equation 2), and (iii) Young modulus for cortical and trabecular bone as function of density (Equations 3 and 4).

$$\rho_{\mathrm{K2HPO4}} = 10^{-3}(a \times \mathrm{HU}) \qquad \left[\mathrm{g/cm^3}\right] \tag{1}$$

$$\rho_{\mathrm{ash}} = .877 \times 1.21 \times \rho_{\mathrm{K2HPO4}} + .08 \qquad \left[\mathrm{g/cm^3}\right] \tag{2}$$

$$E_{\mathrm{cort}} = 10200 \times {\rho_{\mathrm{ash}}}^{2.01} \quad [\mathrm{MPa}]\, \rho_{\mathrm{ash}} \geq .486 \left[\mathrm{g/cm^3}\right] \tag{3}$$

$$E_{\mathrm{trab}} = 2398 \ [\mathrm{MPa}] \qquad .3 < \rho_{\mathrm{ash}} < .486 \left[\mathrm{g/cm^3}\right] \tag{4}$$

Concerning Poisson's ratio, it was set to the constant value $\nu = .3$.[13]

In their work,[13] authors opted for (Equation 1), which has been drawn based on previous experimental studies, giving that CT scans are usually performed without calibration phantoms as it is the case in our work. For ρ_{K2HPO4} calculation, we determined a by solving (Equation 2) for maximum values of ρ_{ash} and HU respectively. HU maximal value is provided by the software, while ρ_{ash} maximal value is determined by solving (Equation 3) where we consider that the maximum value of $E_{\mathrm{cort,max}} = 20\,\mathrm{GPa}$. Based on this method, we obtained $a = .82\,\mathrm{g/cm^3}$ knowing that HU maximal value is 1610. In our study we considered 3 material types; (i) cortical bone with $\rho_{\mathrm{ash}} \geq .486\,[\mathrm{g/cm^3}]$, (ii) trabecular bone

with $.3 < \rho_{ash} < .486\,[g/cm^3]$, and trabecular bone with $\rho_{ash} = .3\,[g/cm^3]$. We affected .3value for low ρ_{ash} and we considered the material as a trabecular bone for simplification.

2.3.2 | Mesh generation

The surface of the proximal femurs is meshed using a semi-automatic mesher in the Materialise 3-Matic software. The bone surface mesh was uniform and composed of 127,604 triangular elements with an edge length of 1.5 mm. The mesh quality in our work has been verified using the "Inspect part" tool where we can regulate the threshold values of the element size then we analyze the mesh quality using the "Analyse mesh quality" tool, where we check if all surface meshes are well done.

For the proximal femur bone, a volume mesh composed of tetrahedral elements was created from the surface mesh. The selected tetrahedral elements are of the quadratic type (C3D10), each having 10 nodes acting as so many interpolation points. These elements are able to describe non-linear behaviors. They are well suited to study the biomechanical behavior of bone tissue[14-16] and are now widely used in biomechanical modeling.

2.4 | Bones mechanical behavior

2.4.1 | Mechanical behavior law

The FE simulations were performed on Abaqus using UMAT subroutine that describes bone behavior law coupled with the biological laws representing the bone remodeling. The algorithm was implemented in language FORTRAN 90.

Cortical bone and trabecular bone were considered as isotropic materials with linear elastic and quasi fragile behavior. The damage resulting from cyclic loadings affects both cortical and cancellous bone properties and subsequently their behavior, potentially leading to the development of micro-cracks and modifications in bone microarchitecture.

In case of high external loading damage could reach its maximal value 1, representing bone fracture/failure.

$$d^{n+1} = d^n + \delta d \tag{5}$$

$$\delta d = \frac{1}{N_f} \tag{6}$$

$$N_f = C\Delta\varepsilon^{-\vartheta} \tag{7}$$

$$\delta d_i = \frac{1}{2.719 \times 10^{-10} \times \Delta\varepsilon_i{}^{-1.2}}$$

$$\varepsilon_{eq} = \sqrt{\frac{2}{3}\varepsilon_{ij}\varepsilon_{ij}} \tag{8}$$

In study, the accumulation of damage at a given cycle d^{n+1} is determined based on (Equation 6). The incremental damage δd_i is expressed based on the number of failure cycles N_f in the i direction (Equations 5 and 6). The latter is expressed in terms of the amplitude of applied micro-strains $\Delta\varepsilon$, which correspond to the equivalent strain ε_{eq} (Equation 8), while C and ϑ are constants obtained experimentally depending on the mechanical solicitation type.[17] Accordingly, damage in case of compression is expressed by (Equation 7).[18,19]

Since there is an empirical relationship between bone density and both Young's modulus and Poisson's ratio, damage has been added to their formulation in (Equations 9 and 11).[18] Young modulus E depends then on its initial value $E_i{}^0$, the incremental damage d_i, and bone density ρ. In (Equation 10) representing the function that characterizes Young's modulus under the variation of bone density ξ, ρ_l is the bone density separating cortical from trabecular bone,

while ξ_c and ξ_s represent respectively the constants defining Young's modulus evolution in the cortical bone and trabecular bone.

In addition to bone density, Poison's ratio ν depends also on its initial values for cortical bone ν_c and trabecular bone ν_s. Concerning (Equation 13), it represents the ramp function. All the mechanical parameters are presented in (Table 3).

$$E = E_i^0(1-d_i)\omega^{\xi(\rho)} \tag{9}$$

$$\xi(\rho) = \xi_s - (\xi_s - \xi_c)S\left(\frac{\rho}{\rho_l} - 1\right) \tag{10}$$

$$\nu(\rho) = \nu_s - (\nu_s - \nu_c)S\left(\frac{\rho}{\rho_l} - 1\right) \tag{11}$$

$$S(x - x_0) = \frac{H(x - x_0)}{x - x_0} \tag{12}$$

$$H(x - x_0) = \frac{(x - x_0) + \mathrm{abs}(x - x_0)}{2} \tag{13}$$

2.4.2 | Mechanical properties

For simulation, the initial values of parameters are presented as follows (Table 1). Where both Young modulus are calculated based on the density obtained from the CT scan images.

2.4.3 | Boundary conditions

The 3D geometry of femurs whether of the patient with and without breast cancer have been exported to be used in the finite element software Abaqus. According to medical reports,[20] low, medium and high physical activities correspond respectively to .79, 1.58, and 2.38 mm of displacement. In the work of reference 17, authors have inflated the values of those displacements to emphasize their effects on bone strength and damage rate throughout life. For the same reason, we chose to inflate the displacement value representing low activity and consider 2 mm of displacement applied on the femoral head with an angle of 19°. Choosing the low activity displacement is due to low activity of elderly patients. The lower surfaces of the proximal femurs have been embedded to prevent bone movement and the mechanical loadings were applied as daily cyclic loadings on the femoral head as shown in (Figure 1).

The loading conditions have been modeled using cyclic patterns. Each cycle involves a compression phase with a 2 mm displacement, succeeded by a relaxation phase, where the displacement above the femoral head is maintained at zero. To reduce the simulation duration, we have conducted 12 cycles over the span of 1 year, with each individual cycle lasting for a duration of 30 days.

TABLE 1 Initial femur mechanical properties.

Patient	Parameter	Value
Proximal femur of healthy women	$E_{\mathrm{cort}}{}^0$	7.37×10^3 MPa
	$E_{\mathrm{trab}}{}^0$	2.39×10^3 MPa
	$\rho_{\mathrm{cort}}{}^0$	.85 g/cm^3
	$\rho_{\mathrm{trab}}{}^0$	.39 g/cm^3

2.5 | Biological behavior

Aiming to determine the mechanical behavior of the proximal femur under primary and secondary breast cancer in addition to BC treatments, several remodeling scenarios over a period of time of 1 year, have been carried out (Figure 2). The initial biological conditions have been directly provided in the code, while the initial mechanical properties of the bone have been called from its initial characteristics assigned by Mimics Materialise software. Within the UMAT code, cells and treatments' concertation, stiffness matrix, bone mechanical properties and the stress are updated.

Detailed description of all bone remodeling models programmed on UMAT subroutine are presented in (Table 2).

From the mathematical models implemented in UMAT, we calculate the BV/TV values, which depends on the bone density value (Equation 17).[21]

$$\rho = 2.31 \times \mathrm{BV/TV} \tag{14}$$

The density values are utilized in the calculation of several parameters, such as Young's modulus and Poisson's ratio, which are then integrated to compute stress, damage, and strain energy density.

For treatments impact on bone remodeling model, we have considered that all the treatments are considered at the same period with a daily administration of drugs and that the initial conditions of the model are those of secondary BC model.

2.6 | Mechanobiological coupling

Based on the work of reference 22, the mathematical model representing the mechanical strains in the extravascular matrix's effect on bone remodeling has been represented by (Equation 17). This function depends principally on the

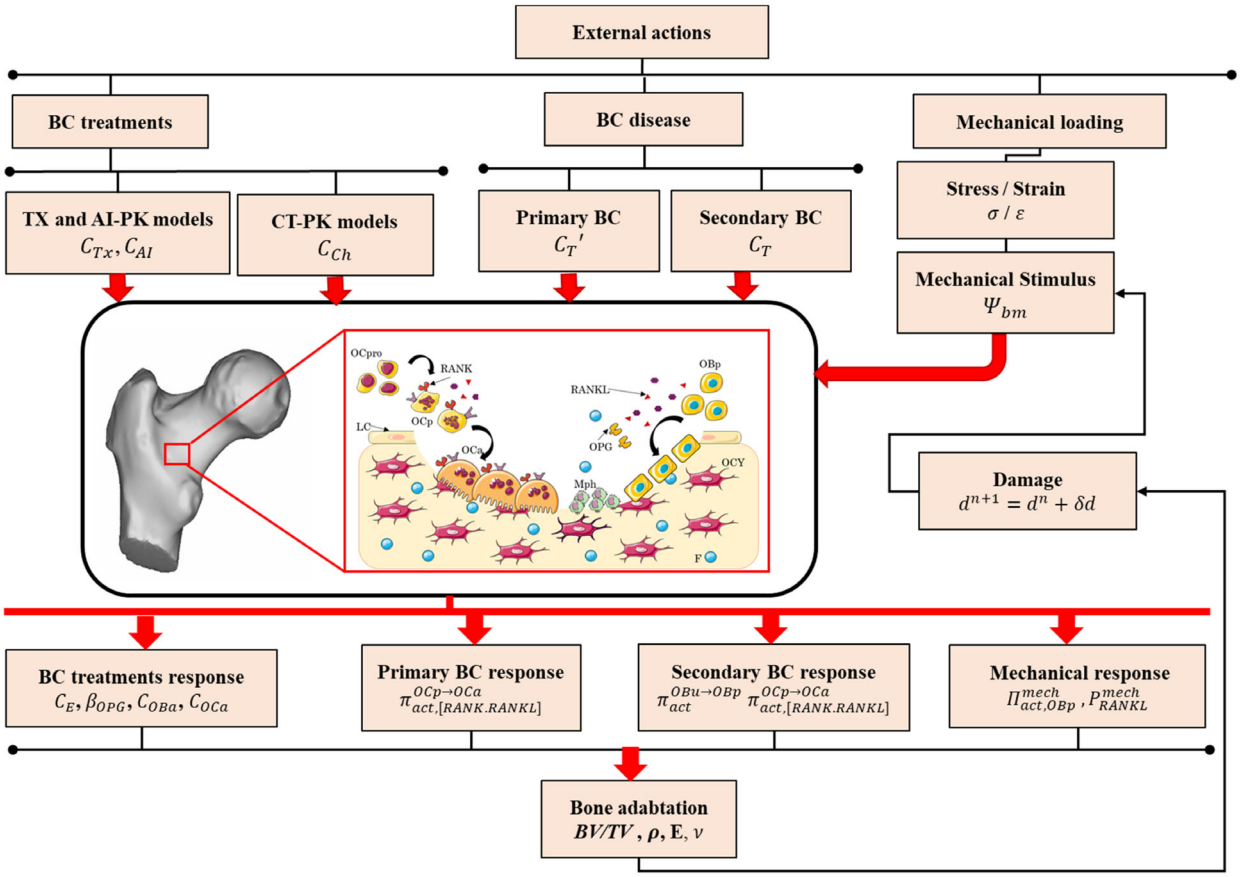

FIGURE 2 Organigram of the bone remodeling algorithm implemented in Abaqus code with UMAT subroutine. Primary BC, secondary BC, and treatments models have been implemented separately, while the mechanical algorithm is the same for all models. For the model of validation, only the mechanical algorithms have been implemented.

mechanical stimulus represented by the strain energy density (SED) Ψ_{bm}. Knowing that SED could be affected by damage (Equation 5), SED calculated basically based on stress σ and strain ε values (Equation 15), has been modified to consider damage in (Equation 16). Due to the mechanical stimulus, preosteoblasts proliferation is controlled by the activation function $\Pi^{\text{mech}}_{\text{act,OBp}}$ (Equation 17), where λ is the anabolic strength parameter, $\widetilde{\Psi_{bm}} = 1 \times 10^{-3}$ MPa, and $\widehat{\Psi_{bm}} = \left(1+\lambda^{-1}\right)\widetilde{\Psi_{bm}}$. The maximum proliferation rate is reached when $\Pi^{\text{mech}}_{\text{act,OBp}} = 1$ and the minimum value is set to $\Pi^{\text{mech}}_{\text{act,OBp}} = 1/2$ relatively to Ψ_{bm} the threshold value above which the proliferation is activated.

Besides the activation function of preosteoblasts' proliferation, we have also considered the influence of mechanical stimulation on RANKL production inhibition. This has been represented by the function $P^{\text{mech}}_{\text{RANKL}}$ proposed by reference 22 (Equation 18), where α is the inhibition parameter of RANKL production (Table 3).

$$w\left(\vec{x}^{(i)}\right) = \frac{1}{2}\sigma\left(\vec{x}^{(i)}\right) : \varepsilon\left(\vec{x}^{(i)}\right) \tag{15}$$

$$\Psi_{bm} = w\left(\vec{x}^{(i)}\right)(1-d_i) \tag{16}$$

$$\Pi^{\text{mech}}_{\text{act,OBp}} = \begin{cases} 1/2 & \Psi_{bm} \le \widetilde{\Psi_{bm}} \\ 1/2\left(1+\lambda\left(\dfrac{\Psi_{bm}}{\widetilde{\Psi_{bm}}}-1\right)\right), & \widetilde{\Psi_{bm}} < \Psi_{bm} \le \widehat{\Psi_{bm}} \\ 1 & \widehat{\Psi_{bm}} \le \Psi_{bm} \end{cases} \tag{17}$$

TABLE 2 Description of all bone remodeling models implemented via UMAT in this study.

Geometrical model	Bone remodeling model	Agent	Modification applied on the model	References
Proximal femur of healthy women	Normal conditions	No agent	No modification	(Appendix A.1)
	Primary BC conditions	Primary BC cells	RANKL concentration OPG concentration IL-6 concentration	(Appendix A.2)
	Secondary BC conditions	Secondary BC cells	Wnt concentration DKK-1 concentration RANKL concentration PTH concentration IL-6 concentration	(Appendix A.3)
	BC treatments conditions	Chemotherapy	OBa concentration OCa concentration	(Appendix A.4)
		Tamoxifen	Estrogen concentration	(Appendix A.4)
		Aromatase Inhibitors	Estrogen concentration	(Appendix A.4)

TABLE 3 Mechanical models parameters.

Parameter	Value	Reference
ξ_s	2.5	18
ξ_c	3.2	18
ν_s	.2	18
ν_c	.32	18
ρ_l	$1.2\,\text{g/cm}^3$	18
λ	1.25	22
α	3.5×10^4 pM/day	22

$$P_{\mathrm{RANKL}}^{\mathrm{mech}} = \begin{cases} \alpha\left(1 - \dfrac{\Psi_{bm}}{\Psi_{bm}(t_0)}\right) & \Psi_{bm} < \widetilde{\Psi_{bm}} \\ 0 & \Psi_{bm} \geq \widetilde{\Psi_{bm}} \end{cases} \tag{18}$$

3 | RESULTS AND DISCUSSION

The numerical simulation of the proposed mechanobiological models was tested and validated by comparing the obtained 3D simulation results notably bone volume fraction results with our previous validated BV/TV results from references 4,11 Bone remodeling computational simulation has been carried out over a one-year-loading period, for the 73-year-old healthy women, under displacements of 2 mm, and under breast cancer and treatment effect as presented in (Table 4).

3.1 | Bone density variation

Figure 3 illustrates the BV/TV variations over a one-year period, simulating the bone remodeling model using MATLAB software, akin to the approach undertaken in a prior study.[4] This presentation is supplemented by the distribution of von Mises stresses within the bone for each configuration, as detailed in (Table 4).

As observed in (Figure 3), the BV/TV changes exhibited a similarity between the effects of secondary breast cancer and BC treatments when comparing the computational model results to the zero-dimensional model. However, a discernable distinction of 5% was evident in the results concerning the effects of primary breast cancer. This variation could potentially be attributed to the amplified impact of mechanical stimulation, which becomes more pronounced with increased bone density. Notably, the bone force applied in the zero-dimensional model was of greater magnitude, solely directed toward promoting bone formation. Conversely, the finite element model incorporated a minor displacement, resulting in the distribution of Strain Energy Density (SED) in a heterogeneous manner across the three-dimensional geometry. Regarding von Mises stress, stress levels decrease with augmented bone loss. This phenomenon can be attributed to the reduced elasticity that accompanies diminishing bone density, thereby leading to reduced stress within the bone microenvironment. Moreover, alterations in the mechanical environment contribute to the suppression of bone formation stimulation, ultimately leading to further degradation of the bone matrix.

Bone density distribution whether in the cortical and trabecular bone has been noticeably impacted by BC and BC treatments. In (Figure 4) primary BC has induced a modest yet perceptible increase in density within both the cortical and trabecular bone after a one-year simulation. In contrast, the impact was more pronounced in the case of secondary BC and treatment regimens, resulting in a discernible reduction in density across both cortical and trabecular bone. This discrepancy in outcomes can be attributed to our deliberate consideration of high-intensity treatment regimens condensed within a relatively short timeframe of 1 year. As a consequence of this approach, the effects of each treatment have been notably amplified, and the cumulative outcome is the result of their accumulation over time. This underscores the intricate relationship between treatment intensity, temporal considerations, and the overall influence

TABLE 4 Models attributed bone remodeling configurations and mechanical conditions.

Geometrical model	Configuration number	Bone remodeling model	Agent	Mechanical conditions
Proximal femur of healthy women	1	Normal conditions	No agent	2 mm displacement applied on femur head, which is embedded in the lower surface
	2	Primary BC conditions	Primary BC cells	
	3	Secondary BC conditions	Secondary BC cells	
	4	BC treatments conditions	Chemotherapy Tamoxifen Aromatase Inhibitors	

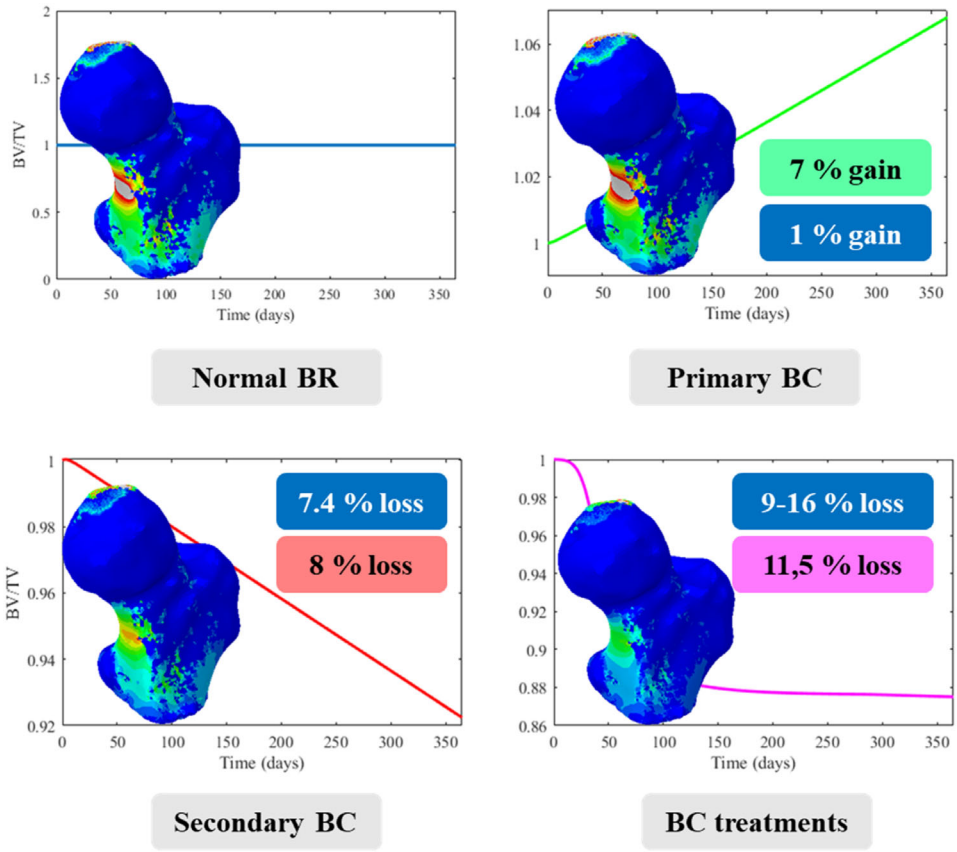

FIGURE 3 von Mises stress variation for the FE modeling and BV/TV variation for the zero-dimension modeling in the four configurations: (i) Normal BR, (ii) BR under primary BC effect, (iii) BR under secondary BC effect, and (iv) BR under Chemotherapy, Tamoxifen, and Aromatase inhibitor effects. BV/TV values in the FE models represent the maximal variation obtained in whole femur. In the BC treatments case, we distinguish between trabecular bone (9% of BV/TV loss) and cortical bone (16% of BV/TV loss). The percentage is calculated based on $(\mathrm{BV/TV}_X - \mathrm{BV/TV}_{\mathrm{Normal}})/\mathrm{BV/TV}_{\mathrm{Normal}}$, where X is the studied condition.

on bone density dynamics. Several studies have yielded critical insights into the intricate relationship between breast cancer (BC), its treatments, and their impact on bone mineral density (Table 5). In one study detailed in reference 23, a group of women newly diagnosed with breast cancer, with the majority being in the early stage and exhibiting positive hormone receptor status, experienced significant improvements in BMD across distinct bone regions: specifically, the lumbar spine, femur neck, and total hip experienced BMD increments of +1.83%, +2.29%, and +3.26%, respectively. Those results were lower than our zero-dimensional model's ones, which indicated a more substantial increase of +7%, while the finite element model displayed a modest 1% of bone gain.

It is worth highlighting the intriguing disparity observed when comparing these results with the predictions from our computational models. Notably, our zero-dimensional model projected a notably more substantial increase in BMD, quantified at +7%. This divergence raises intriguing questions about the underlying factors contributing to the discrepancies between the actual outcomes and the predictions made by the model. One potential factor could be the simplifications inherent in the zero-dimensional model, which might not adequately capture the intricacies of the biological and mechanical interactions occurring within the bone microenvironment. On the other hand, the finite element model displayed a more moderate 1% rise. The small difference between our FE model and the experimental findings could be due to the low mechanical loading conditions, a factor that could have influenced the remodeling process. Furthermore, numerous other factors may contribute to this variation such as the patients' age, overall health, and lifestyle.

In the work of reference 24 the researchers delves into the impact of metastatic cancer, highlighting a concerning −7.69% BMD decrease in cylindrical specimens of patients who underwent excisional biopsy. In a different context, the investigation by reference 25 examines into postmenopausal BC patients with bone metastases. This reveals a −11.1% reduction in BMD in the lumbar spine, along with a more pronounced −17.8% decrease in femoral neck BMD. These

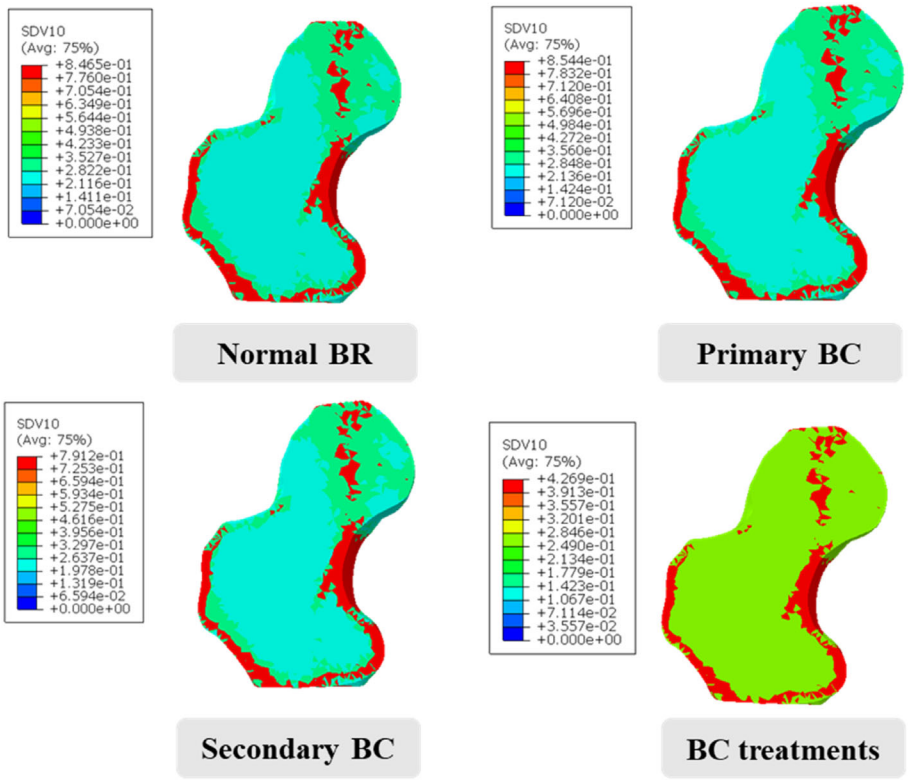

FIGURE 4 Bone density variation in g/cm^3 after 1 year of simulation under the following conditions: (i) Normal BR, (ii) BR under primary BC effect, (iii) BR under secondary BC effect, and (iv) BR under Chemotherapy, Tamoxifen, and Aromatase inhibitor effects.

findings collectively underscore the multifaceted nature of bone health in the presence of cancer. In comparison with the outcomes of our models, there was greater similarity observed with the results presented in reference 24. Conversely, the research described in reference 25 indicated a more pronounced decrease in BMD due to secondary BC. However, it is important to note that the time interval between the onset of metastasis and the measurements in this study was not specified. Therefore, this discrepancy could potentially be attributed to the development of bone metastasis over a substantial span of time for these patients.

Concerning BC treatments effect, further insights emerge from the investigation detailed in article,[26] wherein the lumbar spine BMD decreased by −9.9% following 24 months of aromatase inhibitor treatment, which started after chemotherapy and tamoxifen. Likewise, patients who completed treatment with exemestane, post chemotherapy and tamoxifen, exhibited a −12% decrease in lumbar spine BMD.[26] Over a more extended timeframe, article[27] demonstrates a significant −17.32% decrease in lumbar spine BMD after 5 years of BC treatments, including Anastrozole. Similarly, premenopausal women with receptor-positive breast cancer treated with Anastrozole plus goserelin showed a corresponding −17.32% reduction in lumbar spine BMD.[28] Our finite element model results indicate a notably larger reduction in bone mineral density (BMD), particularly in the cortical bone, where the decrease is substantial at −49%. In contrast, the decrease is comparatively limited to −19.3% in the trabecular bone (Figure 4). These outcomes, specifically related to the cortical bone, highlight significant bone loss compared to the findings from experimental studies. It is important to acknowledge that the marked decrease in our models can be attributed to the inclusion of all treatments simultaneously, as opposed to their distribution over a five-year period. This approach was chosen for two reasons: firstly, to facilitate a direct comparison with the results of other scenarios (primary BC and secondary BC), which were simulated over a single year, and secondly, to evaluate the potential impact of accumulating treatments within the same timeframe on BMD. The implications of these results lead us to the conclusion that the cortical bone is more susceptible to the effects of multiple treatments administered concurrently.

3.2 | Bone mechanical response

In Figure 5, von Mises stress, damage, in addition to the mechanical stimulus has been represented for the four configurations (Table 4) in order to analyze the effect of BC and BC treatment on the mechanical response of the bone.

TABLE 5 Comparative BMD results from the zero-dimensional models[3,4] and experimental studies for primary BC, secondary BC, and BC treatments cases.

	State	Zero-dimension model results	FE Model results	Experimental study result	Experimental study information	References
BMD	Primary BC	+7%	+1%	+1.83%	Lumbar spine of women with newly diagnosed breast cancer	23
				+2.29%	Femur neck of women with newly diagnosed breast cancer	
				+3.26%	Total hip of women with newly diagnosed breast cancer	
	Secondary BC	−8%	−7.4%	−7.69%	Bone cylindrical specimens of patients with metastatic cancer images	24
				−11.1%	Lumbar spine of postmenopausal BC patients suffering from bone metastases	25
				−17.8%	Femoral neck of postmenopausal BC patients suffering from bone metastases	
	BC treatments	−6.49%	−19.3%	−9.9%	Lumbar spine after 24 months of aromatase inhibitor (Anastrozole) treatment following chemotherapy and tamoxifen.	26
				−12%	Lumbar spine of patients after completing treatment with aromatase inhibitor (Exemestane), following chemotherapy and tamoxifen.	
				−17.32%	Lumbar spine of patients after 5 years of BC treatments including Anastrozole	27
				−17.4%	Premenopausal women with receptor-positive breast cancer treated with Anastrozole plus goserelin	28

Figure 5 illustrates that the primary BC's influence on bone mechanical behavior is limited, owing to its minor impact on bone density. However, secondary BC and BC treatments result in diminished stress and SED values, accompanied by an increased level of damage, particularly evident when treatments are applied. The decrease in density contributes to a reduction in the bone's Young's modulus, reflecting a loss of stiffness. Consequently, stress and the energy of deformation stored within the bone decrease.

Research into bone quality under the purview of reference 29 has demonstrated that bone metastasis from prostate and breast cancers significantly affects bone quality. This study identifies notable reductions in vertebral strength and stiffness under these conditions, which supports and justifies our observations in (Figure 5). Another investigation involving mechanical testing on cortical bone samples with metastatic lesions reference 30 reveals that the Young's modulus and yield strength of cortical bone experience significant decreases under compression when compared to cancer-free samples. This reduction underscores the increase in cortical bone ductility due to the progression of osteolysis. Our model arrives also at a similar conclusion, emphasizing that the decrease in Young's modulus contributes to diminished stress generation within the bone matrix, ultimately yielding a lower strain energy density.

When the SED values drop due to bone loss, the positive impact of physical activity on bone health in BC patients undergoing treatments is lost. Moreover, the bone becomes more susceptible to micro-cracks, as evidenced by escalated damage post-treatment (Figure 5). This damage assumes distribution in areas that remained undamaged under

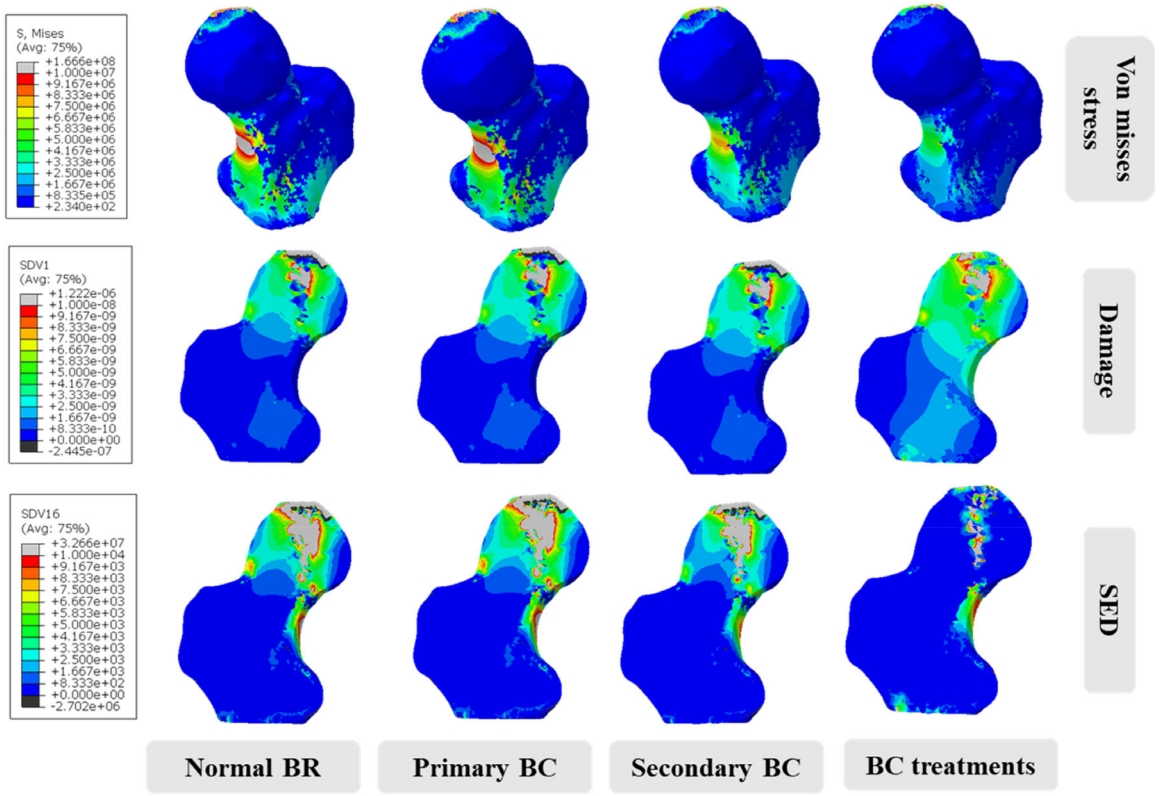

FIGURE 5 von Mises stress, damage, and SED variation for the four configurations: (i) Normal BR, (ii) BR under primary BC effect, (iii) BR under secondary BC effect, and (iv) BR under Chemotherapy, Tamoxifen, and Aromatase inhibitor effects.

equivalent mechanical forces in normal conditions. This observation aligns with a study conducted by [Altered mechanical behavior of demineralized bone following therapeutic radiation], which reveals decreased fatigue strength following therapeutic radiation, thereby negatively affecting bone density. As microcracks propagate and interact, the material's load-bearing capacity diminishes, consequently reducing its fatigue strength. Notably, the impact of treatments is more pronounced compared to secondary BC, considering their application subsequent to BC onset when the bone's strength is compromised. This aligns with multiple studies indicating that bone density decline is more pronounced in patients already exhibiting weakened bone due to factors such as age or diseases.[31]

The overall obtained results indicate that the mechanical behavior of bone is more significantly impacted following secondary breast cancer and treatments. This is evidenced by a noticeable decrease in bone density, resulting in reduced bone stimulation and, consequently, a diminished effect of physical activity on bone recovery.

4 | CONCLUSION

In this paper, we have introduced a finite element model of bone remodeling that incorporates the influence of breast cancer and its treatments on bone's mechanical behavior. Our model successfully emulates the effects of breast cancer and its treatments on bone density. The obtained results underscore the significance of biological conditions in determining bone quality, pinpointing breast cancer and its treatments as key factors influencing the evolution of bone characteristics in patients grappling with the disease. The majority of our results align quantitatively with clinical observations and experimental studies found in the literature. While experimental conditions and patient characteristics vary, our model's outcomes generally fall within a reasonable range of existing literature.

However, it is important to acknowledge that the numerical model employed does possess certain limitations. Most notably, the mineralization process, which is altered due to primary breast cancer, introduces complexities that our model may not fully capture. It is important to recognize that an increase in bone volume after primary breast cancer does not necessarily signify improved matrix quality; rather, it could reflect a bone that is fragile due to a highly

mineralized matrix. Furthermore, we simulated the model over a one-year period, and all treatments were implemented simultaneously. We acknowledge that this approach might amplify treatment effects and not fully capture the nuanced impact of their long-term usage. Additionally, our simulations were conducted using a single femur. However, in our forthcoming studies, we aspire to incorporate multiple femurs and simulate various types of healthy femurs. This endeavor is aimed at broadening the scope and enhancing the applicability of our model.

Despite these limitations, the findings of this study can serve as a foundation for the development of innovative treatments aimed at mitigating bone loss in breast cancer patients. Additionally, the model itself has the potential for further development, possibly leading to the creation of a software tool that physicians can use to predict their patients' long-term bone status. This would be a valuable resource for informed decision-making in clinical practice.

ACKNOWLEDGMENTS

This work was supported by the Partenariat Hubert Curien Franco-Moroccan TOUBKAL (PHC Toubkal) N° TBK/20/102 – CAMPUS N°43681QG.

CONFLICT OF INTEREST STATEMENT

The authors declare no conflicts of interest.

DATA AVAILABILITY STATEMENT

Data sharing not applicable to this article as no datasets were generated or analysed during the current study.

REFERENCES

1. Ait Oumghar I, Barkaoui A, Chabrand P. Toward a mathematical modeling of diseases' impact on bone remodeling: technical review. *Front Bioeng Biotechnol*. 2020;8:1236. 10.3389/fbioe.2020.584198
2. Ait Oumghar I, Barkaoui A, Chabrand P. Mechanobiological behavior of a pathological bone. *Biomechanics and Functional Tissue Engineering*. Intechopen; 2021. doi:10.5772/intechopen.97029
3. Kalder M, Hadji P. Breast cancer and osteoporosis–management of cancer treatment-induced bone loss in postmenopausal women with breast cancer. *Breast Care*. 2014;9(5):312. doi:10.1159/000368843
4. Ait Oumghar I, Barkaoui A, Chabrand P, et al. Experimental-based mechanobiological modeling of the anabolic and catabolic effects of breast cancer on bone remodeling. *Biomech Model Mechanobiol*. 2022;21:1841-1856. doi:10.1007/S10237-022-01623-Z
5. Barkaoui A, Ait Oumghar I, Ben Kahla R. Review on the use of medical imaging in orthopedic biomechanics: finite element studies. *Comput Methods Biomech Biomed Eng Imaging Vis*. 2021;9(5):535-554. doi:10.1080/21681163.2021.1888317
6. Hambli R, Boughattas MH, Daniel JL, Kourta A. Prediction of denosumab effects on bone remodeling: A combined pharmacokinetics and finite element modeling. *J. Mech. Behav. Biomed. Mater.* 2016. doi:10.1016/j.jmbbm.2016.03.010
7. Bolognese MA, Teglbjærg CS, Zanchetta JR, et al. Denosumab significantly increases DXA BMD at both trabecular and cortical sites: results from the FREEDOM study. *J Clin Densitom*. 2013;16(2):147-153. doi:10.1016/J.JOCD.2012.02.006
8. Cummings SR, Martin JS, McClung MR, et al. Denosumab for prevention of fractures in postmenopausal women with osteoporosis. *N Engl J Med*. 2009;361(8):756-765. doi:10.1056/NEJMOA0809493
9. McClung MR, Zanchetta JR, Høiseth A, et al. Denosumab densitometric changes assessed by quantitative computed tomography at the spine and hip in postmenopausal women with osteoporosis. *J Clin Densitom*. 2013;16(2):250-256. doi:10.1016/J.JOCD.2012.02.014
10. Ashrafi M, Gubaua JE, Pereira JT, Gahlichi F, Doblaré M. A mechano-chemo-biological model for bone remodeling with a new mechano-chemo-transduction approach. *Biomech Model Mechanobiol.* 2020;19(6):2499-2523. doi:10.1007/s10237-020-01353-0
11. Ait Oumghar I, Barkaoui A, EL Ghazi A, Chabrand P. Modeling and simulation of bone cells dynamic behavior under the late effect of breast cancer treatments. *Med Eng Phys*. 2023;115(July 2022):103982. doi:10.1016/j.medengphy.2023.103982
12. Lev MH, Gonzalez RG. 17-CT Angiography and CT perfusion imaging. In: Toga AW, Mazziotta JC, eds. *Brain mapping: the methods*. Second ed.), Academic Press; 2002:427-484. doi:10.1016/B978-012693019-1/50019-8
13. Sternheim A, Giladi O, Gortzak Y, et al. Pathological fracture risk assessment in patients with femoral metastases using CT-based finite element methods. *A retrospective clinical study, Bone*. 2018;110:215-220.
14. Polgar K., Viceconti M., & O'Connor J J. A comparison between automatically generated linear and parabolic tetrahedra when used to mesh a human femur. *Proceedings of the Institution of Mechanical Engineers. Part H, Journal of Engineering in Medicine*, 2001;215(1), 85–94. doi:10.1243/0954411011533562
15. Ramos A, Simões JA, Tetrahedral versus hexahedral finite elements in numerical modelling of the proximal femur. *Medical Engineering & Physics*. 2006;28(9):916-924. doi:10.1016/J.MEDENGPHY.2005.12.006
16. Tadepalli SC, Erdemir A, Cavanagh PR. Comparison of hexahedral and tetrahedral elements in finite element analysis of the foot and footwear. *Journal of Biomechanics*. 2011;44(12):2337-2343. doi:10.1016/J.JBIOMECH.2011.05.006
17. Ben Kahla R, Barkaoui A, Merzouki T. Age-related mechanical strength evolution of trabecular bone under fatigue damage for both genders: fracture risk evaluation. *J Mech Behav Biomed Mater*. 2018;84:64-73. doi:10.1016/j.jmbbm.2018.05.006

18. Barkaoui A, RB KAHLA, Merzouki T, Hambli R. Numerical simulation of apparent density evolution of trabecular bone under fatigue loading: Effect of bone initial properties. *J. Mech. Med. Biol.* 2019;19(5). doi:10.1142/S0219519419500416
19. Martin RB, Burr DB, Sharkey NA. *Skeletal tissue mechanics*. Vol 190. Springer; 1998.
20. Barkaoui A, Ben Kahla R, Merzouki T, Hambli R. Age and gender effects on bone mass density variation: finite elements simulation. *Biomech. Model. Mechanobiol.* 2017;16(2). doi:10.1007/s10237-016-0834-x
21. Hernandez CJ, Beaupré GS, Keller TS, Carter DR. The influence of bone volume fraction and ash fraction on bone strength and modulus. *Bone*. 2001;29(1):74-78. doi:10.1016/S8756-3282(01)00467-7
22. Scheiner S, Pivonka P, Hellmich C. Coupling systems biology with multiscale mechanics, for computer simulations of bone remodeling. *Comput Methods Appl Mech Eng*. 2013;254:181-196. doi:10.1016/j.cma.2012.10.015
23. Fraenkel M, Novack V, Mizrakli Y, et al. Bone mineral density in women newly diagnosed with breast cancer: a prospective cohort study. *NPJ Breast Cancer*. 2022;8(1):21. doi:10.1038/S41523-022-00388-Z
24. Nazarian A, Von Stechow D, Zurakowski D, Müller R, Snyder BD. Bone volume fraction explains the variation in strength and stiffness of cancellous bone affected by metastatic cancer and osteoporosis. *Calcif Tissue Int*. 2008;83(6):368-379. doi:10.1007/S00223-008-9174-X
25. Kundaktepe BP, Sozer V, Kundaktepe FO, et al. Association between bone mineral density and bone turnover markers in breast cancer patients and bone-only metastasis. *Medicina (Lithuania)*. 2021;57(9):880. doi:10.3390/medicina57090880
26. Bouvard B, Confavreux CB, Briot K, et al. French recommendations on strategies for preventing and treating osteoporosis induced by adjuvant breast cancer therapies. *Joint Bone Spine*. 2019;86:542-553. doi:10.1016/j.jbspin.2019.07.005
27. Eastell R, Adams JE, Coleman RE, et al. Effect of anastrozole on bone mineral density: 5-year results from the anastrozole, tamoxifen, alone or in combination trial 18233230. *J Clin Oncol*. 2008;26:1051-1057. doi:10.1200/JCO.2007.11.0726
28. Perez EA, Serene M, Durling FC, Weilbaecher K. Aromatase inhibitors and bone loss. *Oncology*. 2006;20(9):1029-1039.
29. Bailey S, Stadelmann MA, Zysset PK, Vashishth D, Alkalay RN. Influence of metastatic bone lesion type and tumor origin on human vertebral bone architecture, matrix quality, and mechanical properties. *J Bone Miner Res*. 2022;37(5):896-907. doi:10.1002/jbmr.4539
30. Kaneko TS, Pejcic MR, Tehranzadeh J, Keyak JH. Relationships between material properties and CT scan data of cortical bone with and without metastatic lesions. *Med Eng Phys*. 2003;25(6):445-454. doi:10.1016/S1350-4533(03)00030-4
31. Cameron DA, Douglas S, Brown JE, Anderson RA. Bone mineral density loss during adjuvant chemotherapy in pre-menopausal women with early breast cancer: is it dependent on oestrogen deficiency? *Breast Cancer Res Treat*. 2010;123(3):805-814. doi:10.1007/s10549-010-0899-7
32. Pivonka P, Zimak J, Smith DW, et al. Model structure and control of bone remodeling: a theoretical study. *Bone*. 2008;43:249-263. doi:10.1016/j.bone.2008.03.025
33. Buenzli P, Pivonka P, Gardiner B, Smith D. Modelling the anabolic response of bone using a cell population model. *Journal of Theoretical Biology*. 2012;307:42-52. doi:10.1016/J.JTBI.2012.04.019

APPENDIX A

A.1 | BONE REMODELING MODEL

The general mathematical model formulation of bone cell behavior is presented as follows, where the bone cells involved are: Osteoblast precursors (OBp), active osteoblast (OBa), and active osteoclasts (OCa)[22,32]:

$$\begin{cases} \dfrac{dC_{\mathrm{OBp}}(t)}{dt} = D_{\mathrm{OBu}}\pi_{\mathrm{act}}^{\mathrm{OBu}\rightarrow\mathrm{OBp}} C_{\mathrm{OBu}} + \mathcal{P}_{\mathrm{OBp}}\Pi_{\mathrm{act,OBp}}^{\mathrm{mech}} C_{\mathrm{OBp}} - D_{\mathrm{OBp}}\pi_{\mathrm{rep,TGF\beta}}^{\mathrm{OBp}\rightarrow\mathrm{OBa}} C_{\mathrm{OBp}} \\ \dfrac{dC_{\mathrm{OBa}}(t)}{dt} = D_{\mathrm{OBp}}\pi_{\mathrm{rep,TGF\beta}}^{\mathrm{OBp}\rightarrow\mathrm{OBa}} C_{\mathrm{OBp}} - A_{\mathrm{OBa}} C_{\mathrm{OBa}} \\ \dfrac{dC_{\mathrm{OCa}}(t)}{dt} = D_{\mathrm{OCp}}\pi_{\mathrm{act,[RANK.RANKL]}}^{\mathrm{OCp}\rightarrow\mathrm{OCa}} C_{\mathrm{OCp}} - A_{\mathrm{OCa}}\pi_{\mathrm{act,TGF\beta}}^{\mathrm{OCa}\rightarrow +} C_{\mathrm{OCa}} \end{cases} \tag{A1A3}$$

C_{OBu}, C_{OBp}, C_{OBa}, C_{OCp}, C_{OCa} represent respectively OBu, OBp, OBa, OCp, and OCa concentrations.D_{OBu}, D_{OBp}, and D_{OCp} are respectively differentiation rates of OBu, OBp, and OCp.$\mathcal{P}_{OBp}$ is the proliferation rate of the OBp and A_{OBa} and A_{OCa} represent respectively the apoptosis rates of OBa and OCa.

TABLE A1 Description of the biochemical and mechanical factors' integration into the normal BR model.[3]

Factor	Function	Factor concentration
TGFβ	$\pi_{act}^{OBu\to OBp}=\left(\pi_{act,TGF\beta}^{OBu\to OBp}+\pi_{act,Wnt}^{OBu\to OBp}\right)+\left(\pi_{act,TGF\beta}^{OBu\to OBp}\pi_{act,Wnt}^{OBu\to OBp}\right)$	$C_{TGF\beta}=\frac{\alpha k_{res}C_{OCa}+S_{TGF\beta}}{\widetilde{D_{TGF\beta}}}$
Wnt		$C_{Wnt}=\frac{\beta_{Wnt}\pi_{rep,DKK1}}{\widetilde{D_{Wnt}}}$
DKK-1		$C_{DKK1}=\frac{\beta_{DKK1}C_{OBa}}{\widetilde{D_{DKK1}}}$
RANK/RANKL/OPG	$\pi_{act,[RANK.RANKL]}^{OCp\to OCa}=\frac{C_{OCp,[RANK.RANKL]}}{K_{act,[RANK.RANKL]}^{OCp\to OCa}+C_{OCp,[RANK.RANKL]}}$	$C_{OCp,[RANK.RANKL]}=K_{a,[RANK.RANKL]}C_{RANKL}C_{OCp,RANK}$ $C_{OCp,RANK}=\rho_{OCp,RANK}C_{OCp}$ $C_{RANKL}=\frac{C_{RANKLmax}}{\left(1+K_{A1,OPG}C_{OPG}+K_{A2,RANK}C_{OCp,RANK}\right)}$ $\left(\frac{\beta_{OBp,RANKL}+P_{RANKL}^{mech}}{\beta_{OBp,RANKL}+\widetilde{D_{RANKL}C_{RANKLmax}}}\right)$ $C_{RANKLmax}=R_{RL,OBp}C_{OBp}\pi_{RANKL}^{Ligand}$ $C_{OPG}=\frac{\left(\beta_{OBa,OPG}C_{OBa}\right)\pi_{OPG}^{Ligand}}{\frac{\left(\beta_{OBa,OPG}C_{OBa}\right)\pi_{rep,OPG}^{Ligand}}{C_{OPGmax}}+\widetilde{D_{OPG}}}$ $P_{RANKL}^{mech}=\begin{cases}\alpha\left(1-\frac{\Psi_{bm}}{\Psi_{bm}(t_0)}\right), & \Psi_{bm}<\Psi_{bm}(t_0)\\ 0 & \Psi_{bm}\geq\Psi_{bm}(t_0)\end{cases}$
PTH, IL-6	$\pi_{RANKL}^{Ligand}=\left(\pi_{act,RANKL}^{PTH}+\pi_{act,RANKL}^{IL6}+\pi_{rep,RANKL}^{E}\right)+\left(\pi_{act,RANKL}^{PTH}\pi_{rep,RANKL}^{E}\right)-\left(\pi_{act,RANKL}^{PTH}\pi_{act,RANKL}^{IL6}\right)$ $\pi_{OPG}^{Ligand}=\left(\pi_{rep,OPG}^{PTH}+\pi_{rep,OPG}^{IL6}+\pi_{act,OPG}^{E}\right)+\left(\pi_{rep,OPG}^{PTH}\pi_{act,OPG}^{E}\right)-\left(\pi_{rep,OPG}^{PTH}\pi_{rep,OPG}^{IL6}\right)$	$C_{PTH}=\frac{\beta_{PTH}}{\widetilde{D_{PTH}}}$ $C_{IL6}=\frac{\left(\beta_{IL6}C_{OBu}\right)\pi_{act,TGF}^{IL6}}{\frac{\left(\beta_{IL6}C_{OBu}\right)\pi_{act,TGF}^{IL6}}{C_{IL6max}}+\widetilde{D_{IL6}}}$ $C_E=9.175\times10^2\,\mathrm{pM}$ (healthy women)
Mechanical	$\Pi_{act,OBp}^{mech}=\begin{cases}\frac{1}{2} & \Psi_{bm}\leq\Psi_{bm}(t_0)\\ \frac{1}{2}\left(1+\lambda\left(\frac{\Psi_{bm}}{\Psi_{bm,min}}-1\right)\right), & \Psi_{bm}(t_0)<\Psi_{bm}\leq\widehat{\Psi_{bm}}\\ 1 & \widehat{\Psi_{bm}}\leq\Psi_{bm}\end{cases}$	$\Psi_{bm}=\Psi_{bm}(\Sigma,c_{bm},(1-BV/TV))$ $\widehat{\Psi_{bm}}=\left(1+\lambda^{-1}\right)\Psi_{bm}(t_0)$

The Hill activation and repression functions $\pi_{\mathrm{act},X}$ and $\pi_{\mathrm{rep},X}$ used in the model are generally expressed as follows:

$$\pi_{\mathrm{act},X} = \frac{C_X}{K_{\mathrm{act}} + C_X}$$
$$\pi_{\mathrm{rep},X} = \frac{K_{\mathrm{rep}}}{K_{\mathrm{rep}} + C_X} \tag{A4}$$

where C_X is the concentration of the ligand X governing the cellular response, and K_{act} and K_{rep} are respectively the activation and repression constants. The cellular response to different ligands of the model parameters are grouped in (Table A1). In (Tables A1–A3), for each factor X, β_X: production rate, $\tilde{D_X}$: degradation rate, C_X: concentration of X, C_{Xmax}: concentration maximum de X, $K_{a,X}$: association binding rate of its ligand, and $K_{act,X}$ and $K_{rep,X}$: association and repression Hill constants respectively used for the studied factors Hill functions. For Wnt production, it depends on the time at which Wnt production rate increases because of cancer t_{Wnt} and the duration of this increase τ_{Wnt} respectively.[33]

Concerning $\Pi^{\mathrm{mech}}_{\mathrm{act,OBp}}$, it is a function representing the ability of mechanical strains to promote preosteoblasts' proliferation.

The fraction of extravascular bone matrix BV/TV behavior is determined by (Equation A5). BV/TV depends on active osteoblasts and osteoclasts' concentrations, where k_{form} and k_{res} represent respectively the daily volume of bone matrix formed by osteoblast and the daily volume of bone matrix resorbed by osteoclast.

$$\frac{d\mathrm{BV/TV}(t)}{dt} = (k_{\mathrm{form}} C_{\mathrm{OBa}} - k_{\mathrm{res}} C_{\mathrm{OCa}}) \tag{A5}$$

A.2 | PRIMARY BREAST CANCER EFFECT

To mimic the primary BC effect, RANKL, IL-6, and OPG production by osteoblasts have been altered (see Table A2). Where $L_{\mathrm{EV,RANKL}}$ is the ratio of RANKL increase under primary BC effect, $L_{\mathrm{EV,OPG}}$ is the ratio of OPG increase under primary BC effect, and $L_{\mathrm{EV,IL6}}$ is the ratio of IL-6 increase under primary BC effect.

In Table A2 each of $F_{\mathrm{EV,RANKL}}$,$F_{\mathrm{EV,OPG}}$ and $F_{\mathrm{EV,IL6}}$ depends on BC cells' concentration in the breast environment $C_{T'}$. In the following equation, we represent the differential equation of tumor cells concentration evolution over time (Equation A6).

$$\frac{dC_{T'}(t)}{dt} = P_{T'} \pi^{T'}_{\mathrm{act},E} \ln\left(\frac{C_{T'\max}}{C_{T'}}\right) C_{T'} \tag{A6}$$

The activation function of tumor proliferation $\pi^{T'}_{\mathrm{act},E}$ is the Hill action function of E, $P_{T'}$ is the proliferation rate of primary BC cells, and $C_{T'\max}$ is the carrying capacity of primary BC cells concentration.

TABLE A2 Description of the biochemical factors' integration modification in the BR model under primary BC.[3]

Original function	Modified function
$\boldsymbol{C_{\mathrm{RANKLmax}} = R_{\mathrm{RL,OBp}} C_{\mathrm{OBp}} \pi^{\mathrm{Ligand}}_{\mathrm{RANKL}}}$	$C_{\mathrm{RANKLmax}} = R_{\mathrm{RL,OBp}} C_{\mathrm{OBp}} \pi^{\mathrm{Ligand}}_{\mathrm{RANKL}} \boldsymbol{F_{\mathrm{EV,RANKL}}}$ $\boldsymbol{F_{\mathrm{EV,RANKL}}} = L_{\mathrm{EV,RANKL}} C_{T'}$
$\boldsymbol{C_{\mathrm{OPG}} = \frac{(\beta_{\mathrm{OBa,OPG}} C_{\mathrm{OBa}}) \pi^{\mathrm{Ligand}}_{\mathrm{OPG}}}{\frac{(\beta_{\mathrm{OBa,OPG}} C_{\mathrm{OBa}}) \pi^{\mathit{Ligand}}_{\mathit{rep,OPG}}}{C_{\mathrm{OPGmax}}} + \widetilde{D_{\mathrm{OPG}}}}}$	$C_{\mathrm{OPG}} = \frac{(\beta_{\mathrm{OBa,OPG}} C_{\mathrm{OBa}}) \pi^{\mathrm{Ligand}}_{\mathrm{OPG}} \boldsymbol{F_{\mathrm{EV,OPG}}}}{\frac{(\beta_{\mathrm{OBa,OPG}} C_{\mathrm{OBa}}) \pi^{\mathrm{Ligand}}_{\mathrm{rep,OPG}} \boldsymbol{F_{\mathrm{EV,OPG}}}}{C_{\mathrm{OPGmax}}} + \widetilde{D_{\mathrm{OPG}}}}}$ $F_{\mathrm{EV,OPG}} = L_{\mathrm{EV,OPG}} / C_{T'}$
$\boldsymbol{C_{\mathrm{IL6}} = \frac{(\beta_{\mathrm{IL6}} C_{\mathrm{OBa}}) \pi^{\mathrm{IL6}}_{\mathrm{act,TGF}}}{\frac{(\beta_{\mathrm{IL6}} C_{\mathrm{OBa}}) \pi^{\mathrm{IL6}}_{\mathrm{act,TGF}}}{C_{\mathrm{IL6max}}} + \widetilde{D_{\mathrm{IL6}}}}}$	$C_{\mathrm{IL6}} = \frac{(\beta_{\mathrm{IL6}} C_{\mathrm{OBa}}) \pi^{\mathrm{IL6}}_{\mathrm{act,TGF}} \boldsymbol{F_{\mathrm{EV,IL6}}}}{\frac{(\beta_{\mathrm{IL6}} C_{\mathrm{OBa}}) \pi^{\mathrm{IL6}}_{\mathrm{act,TGF}} \boldsymbol{F_{\mathrm{EV,IL6}}}}{C_{\mathrm{IL6max}}} + \widetilde{D_{\mathrm{IL6}}}}}$ $\boldsymbol{F_{\mathrm{EV,IL6}}} = L_{\mathrm{EV,IL6}} C_{T'}$
$\boldsymbol{C_E = \text{constant}}$	$C_E = 8.151 \times 10^1$ pM (postmenopausal women)

TABLE A3 Description of biochemical factors incorporation in the BR model under metastatic breast cancer.[3]

Original function	Modified function
$C_{\mathbf{Wnt}} = \frac{\beta_{\mathbf{Wnt}} \cdot \pi_{\mathbf{rep,DKK1}}}{D_{\mathbf{Wnt}}}$	$C_{\mathrm{Wnt}} = \frac{(\beta_{\mathrm{Wnt}} + \boldsymbol{\beta_{\mathbf{Wnt},T} C_T}) \pi_{\mathrm{rep,DKK1}}}{D_{\mathrm{Wnt}}}$
	$\boldsymbol{\beta_{\mathbf{Wnt},T}} = \boldsymbol{\beta^{\mathbf{max}}_{\mathbf{Wnt},T}} \frac{e^{(t-t_{\mathbf{Wnt}})/\tau_{\mathbf{Wnt}}} + \boldsymbol{\beta^{\mathbf{min}}_{\mathbf{Wnt},T}} / \boldsymbol{\beta^{\mathbf{max}}_{\mathbf{Wnt},T}}}{e^{(t-t_{\mathbf{Wnt}})/\tau_{\mathbf{Wnt}}} + 1}$
$C_{\mathbf{DKK1}} = \frac{\beta_{\mathbf{DKK1}} \cdot C_{\mathbf{OBa}}}{D_{\mathbf{DKK1}}}$	$C_{\mathrm{DKK1}} = \frac{\boldsymbol{\beta_{\mathbf{DKK1},T} C_T}}{D_{\mathrm{DKK1}}}$
$\boldsymbol{\beta_{\mathbf{RANKL}}} = \boldsymbol{\beta_{\mathbf{OBp,RANKL}}}$	$\beta_{\mathrm{RANKL}} = \beta_{\mathrm{OBp,RANKL}} + \boldsymbol{\beta_{T,\mathbf{RANKL}}}$
	$C_{\mathrm{RANKLmax}} = (R_{\mathrm{OBp}} C_{\mathrm{OBp}} + \boldsymbol{R_T C_T}) \pi^{\mathrm{Ligand}}_{\mathrm{RANKL}}$
$C_{\mathbf{PTH}} = \frac{\beta_{\mathbf{PTH}}}{D_{\mathbf{PTH}}}$	$C_{\mathrm{PTH}} = \frac{\beta_{\mathrm{PTH}} + \boldsymbol{\beta_{\mathbf{PTHrP}} C_T \pi^{\mathbf{PTHrP}}_{\mathbf{act,TGF}}}}{D_{\mathrm{PTH}}}$
$C_{\mathbf{IL6}} = \frac{(\beta_{\mathbf{IL6}} C_{\mathbf{OBa}}) \pi^{\mathbf{IL6}}_{\mathbf{act,TGF}}}{\frac{(\beta_{\mathbf{IL6}} C_{\mathbf{OBa}}) \pi^{\mathbf{IL6}}_{\mathbf{act,TGF}}}{C_{\mathbf{IL6max}}} + D_{\mathbf{IL6}}}$	$C_{\mathrm{IL6}} = \frac{(\beta_{\mathrm{IL6,OBa}} C_{\mathrm{OBa}} + \boldsymbol{\beta_{\mathbf{IL6},T} C_T}) \pi^{\mathrm{IL6}}_{\mathrm{act,TGF}}}{\frac{(\beta_{\mathrm{IL6,OBa}} C_{\mathrm{OBa}} + \boldsymbol{\beta_{\mathbf{IL6},T} C_T}) \pi^{\mathrm{IL6}}_{\mathrm{act,TGF}}}{C_{\mathrm{IL6\,max}}} + D_{\mathrm{IL6}}}$
$C_E = \mathbf{constant}$	$C_E = 8.151 \times 10^1$ pM
	(postmenopausal women)

A.3 | SECONDARY BREAST CANCER EFFECT

In this model, each of DKK-1, Wnt, PTHrP, and IL-6 are synthetized by BC tumor cells (Table A3). BC cells' concentration in the bone microenvironment C_T is determined by (Equation A7).

$$\frac{dC_T(t)}{dt} = X_T C_{T'\max} + P_T \pi^T_{\mathrm{act}} \ln\left(\frac{C_{T\max}}{C_T}\right) C_T \tag{A7}$$

X_T is the migration rate of primary BC cells, P_T is the proliferation rate of metastatic BC cells, and C_{Tmax} is the carrying capacity of secondary BC cells concentration.

The activation function of tumor proliferation π^T_{act} depends on the Hill action function assembling the effect of TGF_β, Wnt, RANK-RANKL, and estrogen (E) (Equation A8).

$$\begin{aligned}\pi^T_{\mathrm{act}} = &\left[\left(\pi^T_{\mathrm{act,TGF}} + \pi^T_{\mathrm{act,Wnt}} + + \pi^T_{\mathrm{act,IL6}} + \pi^T_{\mathrm{act},E} + \pi^T_{\mathrm{act,[RANK.RANKL]}}\right] - \left[\left(\pi^T_{\mathrm{act,TGF}} \pi^T_{\mathrm{act,Wnt}}\right) + \left(\pi^T_{\mathrm{act,TGF}} \pi^T_{\mathrm{act,IL6}}\right) + \left(\pi^T_{\mathrm{act,TGF}} \pi^T_{\mathrm{act},E}\right)\right. \\ &+ \left(\pi^T_{\mathrm{act,TGF}} \pi^T_{\mathrm{act,[RANK.RANKL]}}\right) + \left(\pi^T_{\mathrm{act,Wnt}} \pi^T_{\mathrm{act,IL6}}\right) + \left(\pi^T_{\mathrm{act,Wnt}} \pi^T_{\mathrm{act},E}\right) + \left(\pi^T_{\mathrm{act,Wnt}} \pi^T_{\mathrm{act,[RANK.RANKL]}}\right) + \left(\pi^T_{\mathrm{act,IL6}} \pi^T_{\mathrm{act},E}\right) \\ &\left. + \left(\pi^T_{\mathrm{act,IL6}} \pi^T_{\mathrm{act,[RANK.RANKL]}}\right) + \left(\pi^T_{\mathrm{act},E} \pi^T_{\mathrm{act,[RANK.RANKL]}}\right)\right.\end{aligned} \tag{A8}$$

A.4 | BREAST CANCER TREATMENTS EFFECT

A.4.1. | PK models

In order to implement the drugs effect on the bone remodeling affected by breast cancer (Tables A1 and A3) we opted for PK-PD models.[4] In this section, we define the PK models relatively to chemotherapy, tamoxifen, and the aromatase inhibitor. The parameters used in those PK models are represented in (Table A4).

Chemotherapy drug concentration in the blood plasma is determined based on the PK model (Equation A9):

$$\frac{dC_{\mathrm{Ch}}(t)}{dt} = k_{a,\mathrm{Ch}} D_{\mathrm{Ch}} - k_{e,\mathrm{Ch}} C_{\mathrm{Ch}} \tag{A9}$$

TABLE A4 Parameters of pharmacokinetic and pharmacodynamic models of chemotherapy, tamoxifen, and aromatase inhibitors.[4]

	Chemotherapy			Tamoxifen			Aromatase inhibitor		
	Parameter	**Value**	**Description**	**Parameter**	**Value**	**Description**	**Parameter**	**Value**	**Description**
Pharmacokinetic	m_{Ch}	$40\,\mathrm{mg/m^2}$	Mass of the ixabepilone	m_{Tx}	20 mg	Mass of the tamoxifen	m_{AI}	25 mg	Mass of the aromatase inhibitor
	M_{Ch}	506,69 g/mol	Molar mass of ixabepilone	M_{Tx}	371.5 g/mol	Molar mass of tamoxifen	M_{AI}	296,403 g/mol	Molar mass of aromatase inhibitor
	$k_{a,\mathrm{Ch}}$	$6.93 \times 10^{-2}\,1/\mathrm{h}$	Absorption rate of ixabepilone	$k_{a,\mathrm{Tx}}$	$0.7\,1/\mathrm{h}$	Administration rate of tamoxifen	$V_{\mathrm{AI}}/F_{\mathrm{AI}}$	844 L	Volume of tamoxifen administration/ bioavaibility constant
	$k_{e,\mathrm{Ch}}$	$9.6 \times 10^{-3}\,1/\mathrm{h}$	Elimination rate of ixabepilone	$k_{12,\mathrm{Tx}}$	$7.07 \times 10^{-3}\,1/\mathrm{h}$	Tamoxifen transformation rates into N-desmethyl-tamoxifen	$k_{a,\mathrm{AI}}$	$1.13 \times 10^{-2}\,1/\mathrm{h}$	Administration rate of aromatase inhibitor
				$k_{13,\mathrm{Tx}}$	$5.49 \times 10^{-5}\,1/\mathrm{h}$	Tamoxifen transformation rates into 4-hydroxy-tamoxifen	$k_{12,\mathrm{AI}}$	$9.08 \times 10^{-3}\,1/\mathrm{h}$	Aromatase inhibitor transfer rate into the other organs
				$k_{e,\mathrm{Tx}}$	$8 \times 10^{-3}\,1/\mathrm{h}$	Elimination rate of tamoxifen	$k_{13,\mathrm{AI}}$	$3.48 \times 10^{-3}\,1/\mathrm{h}$	Aromatase inhibitor transfer rate into the other organs
				$V_{\mathrm{Tx}}/F_{\mathrm{Tx}}$	724 L	Volume of tamoxifen administration /tamoxifen bioavaibility	$k_{e,\mathrm{Tx}}$	$1.47 \times 10^{-2}\,1/\mathrm{h}$	Elimination rate of aromatase inhibitor
Pharmacodynamic	v_T	$9 \times 10^2\,1/\mathrm{day}$	Kill rate of cancer cells	ρ_{ER}	1000	ER number expressed by OBa	$K_{\mathrm{rep,AI}}$	22.1 pg/mL	Repression constant of aromatase inhibitors
	v_C	$1.8 \times 10^2\,1/\mathrm{day}$	Kill rate of osteoclasts	β_E	$1.95 \times 10^2\,\mathrm{pM/day}$	Production rate of estrogen	λ_{AI}	3.3×10^{-4}	Efficacy factor of aromatase
	v_B	$90\,1/\mathrm{day}$	Kill rate of osteoblasts	$\tilde{D_E}$	$0.01\,1/\mathrm{day}$	Degradation rate of estrogen			
	x_O	$1.32 \times 10^3\,1/\mathrm{mol.L}$	Chemotherapeutic efficacy rate on cancer and bone cells	C_{Eb}	54.86 pg/mL	Initial maximum concentrations of estrogen			

TABLE A4 (Continued)

Chemotherapy			Tamoxifen			Aromatase inhibitor		
Parameter	**Value**	**Description**	**Parameter**	**Value**	**Description**	**Parameter**	**Value**	**Description**
			δ	0.001	Factor of tamoxifen binding to estrogen			
			$K_{a,[\mathrm{ER}.E]}$	1.083 1/pM	Association binding constants of E-ER			
			$K_{a,[\mathrm{Tx}.E]}$	4.5×10^6 1/M.s	Association binding constants of E-Tx			
			λ_{Tx}	0.1	Efficacy factor of tamoxifen			

where, $D_{Ch} = m_{Ch}/M_{Ch}$ is the continuous dose rate of chemotherapy drug, C_{Ch} is the concentration of ixabepilone in the blood plasma, and $k_{a,Ch}$ and $k_{e,Ch}$ are respectively the absorption and elimination rates of ixabepilone by the blood.

Tamoxifen drug concentration in the blood plasma is determined based on the PK model (Equation A10):

$$\frac{dC_{\mathrm{Tx}}(t)}{dt} = k_{a,\mathrm{Tx}} \frac{m_{\mathrm{Tx}}}{M_{\mathrm{Tx}}} \frac{F_{\mathrm{Tx}}}{V_{d,\mathrm{Tx}}} - (k_{12,\mathrm{Tx}} + k_{13,\mathrm{Tx}} + k_{e,\mathrm{Tx}}) C_{\mathrm{Tx}} \tag{A10}$$

where, m_{Tx} is the mass of the tamoxifen taken by the patient, M_{Tx} is the molar mass of tamoxifen, $V_{d,Tx}$ is the volume of tamoxifen administration, F_{Tx} is the tamoxifen bioavaibility constant, $k_{a,Tx}$ is the administration rate of tamoxifen, $k_{12,Tx}$ and $k_{13,Tx}$ are respectively tamoxifen transformation rates into N-desmethyl-tamoxifen and 4-hydroxy-tamoxifen, and finally $k_{e,Tx}$ is the elimination rate of tamoxifen.

Aromatase inhibitor drug concentration in the blood plasma is determined based on the PK model (Equation A11):

$$\frac{dC_{\mathrm{AI}}(t)}{dt} = k_{a,\mathrm{AI}} \frac{m_{\mathrm{AI}}}{M_{\mathrm{AI}}} \frac{F_{\mathrm{AI}}}{V_{d,\mathrm{AI}}} - (k_{12,\mathrm{AI}} + k_{13,\mathrm{AI}} + k_{e,\mathrm{AI}}) C_{\mathrm{AI}} \tag{A11}$$

where, m_{AI} is the mass of the aromatase inhibitor taken by the patient, M_{AI} is the molar mass of aromatase inhibitor, $V_{d,AI}$ is the volume of tamoxifen administration, F_{AI} is the bioavaibility constant, $k_{a,AI}$ is the administration rate of aromatase inhibitor, $k_{12,AI}$ and $k_{13,AI}$ are respectively aromatase inhibitor transfer into the other organs/compartments rates, and finally $k_{e,AI}$ is the elimination rate of aromatase inhibitor.

A.4.2. | PD models

Concerning the PD models, the parameters used are represented in (Table A4).

To represent chemotherapy effect on BC cells, osteoblasts and osteoclasts, the following equations are used (Equations A12–A14).

$$\varepsilon_T(t) = v_T\left(\left(1 - e^{-x_O C_{\mathrm{Ch}}}\right)\right) \tag{A12}$$

$$\varepsilon_C(t) = v_C\left(\left(e^{-x_O C_{\mathrm{Ch}}} - 1\right)\right) \tag{A13}$$

$$\varepsilon_B(t) = v_B\left(\left(e^{-x_O C_{\mathrm{Ch}}} - 1\right)\right) \tag{A14}$$

ε_B and ε_C are respectively the efficacy of chemotherapy on osteoblasts and osteoclasts, and ε_T is the efficacy of chemotherapy on BC cells.v_B, v_C, and v_T are respectively the kill rate of osteoblasts, osteoclasts and cancer cells, while x_O is the chemotherapeutic efficacy rate on cancer and bone cells.

The new bone remodeling and BC cancer model under chemotherapy will be then expressed as follows:

$$\frac{dC_{\mathrm{OBa}}(t)}{dt} = D_{\mathrm{OBp}} \pi_{\mathrm{rep,TGF\beta}}^{\mathrm{OBp}\rightarrow\mathrm{OBa}} C_{\mathrm{OBp}} - A_{\mathrm{OBa}} C_{\mathrm{OBa}} - \boldsymbol{\varepsilon_B C_{OBa}} \tag{A15}$$

$$\frac{dC_{\mathrm{OCa}}(t)}{dt} = D_{\mathrm{OCp}} \pi_{\mathrm{act,[RANK.RANKL]}}^{\mathrm{OCp}\rightarrow\mathrm{OCa}} C_{\mathrm{OCp}} - A_{\mathrm{OCa}} \pi_{\mathrm{act,TGF\beta}}^{\mathrm{OCa}\rightarrow\dagger} C_{\mathrm{OCa}} - \boldsymbol{\varepsilon_C C_{OCa}} \tag{A16}$$

$$\frac{dC_T(t)}{dt} = P_T \pi_{\mathrm{act}}^{E} \ln\left(\frac{C_{T\max}}{C_T}\right) C_T - \boldsymbol{\varepsilon_T C_T} \tag{A17}$$

The effect of tamoxifen and aromatase inhibitor on estrogen has been represented by the following equations:

$$C_{[\mathrm{ER.E}]} = K_{a,[\mathrm{ER.E}]} C_{\mathrm{ER}} C_E \tag{A18}$$

$$C_{\mathrm{ER}} = \rho_{\mathrm{ER}} C_{\mathrm{OBa}} \tag{A19}$$

$$C_E = \frac{C_{E\max}}{\left(1 + K_{a,[\mathrm{Tx.E}]} C_{\mathrm{Tx}} \delta + K_{a,[\mathrm{ER.E}]} C_{\mathrm{ER}}\right)} \quad \frac{\beta_E}{\beta_E + \widetilde{D_E} C_{E\max}}\Bigg) \tag{A20}$$

$$C_{E\max} = C_{\mathrm{Eb}} \pi^E_{\mathrm{rep}} \tag{A21}$$

$$S^E_{\mathrm{rep,TX}} = 1 - \frac{C_{\mathrm{Tx}} - C_{\mathrm{Txmax}}}{C_{\mathrm{Txmin}} - C_{\mathrm{Txmax}}} \tag{A22}$$

$$\pi^E_{\mathrm{rep,AI}} = \left(\frac{K_{\mathrm{rep,AI}}}{C_{\mathrm{AI}} + K_{\mathrm{rep,AI}}}\right)^{0.8} \tag{A23}$$

$C_{[ER.E]}$, C_E, C_{ER} define respectively E-ER concentration, E concentration and ER concentration. $S^E_{rep,TX}$ and $\pi^E_{rep,AI}$ are respectively the efficacy function of tamoxifen and the Hill repression function of aromatase inhibitors on E production. $K_{a,[ER.E]}$ and $K_{a,[Tx.E]}$ are respectively the association binding constants of E-ER and E-Tamoxifen, $K_{rep,AI}$ is the Hill repression constant of aromatase inhibitors, ρ_{ER} is the number of ER expressed by OBa, δ is the factor of tamoxifen binding to estrogen, β_E and $\tilde{D_E}$ are respectively the production and the degradation rates of E, C_{Emax} and C_{Txmax} are the maximum concentrations of E and tamoxifen, while C_{Txmin}, is the minimum concentrations of tamoxifen.